Supporting Information

Enhancing bipolar ion storage in azulene-based conjugated microporous polymer cathodes via donor-acceptor dipole homogenization

Sijie Chen†, Ju Duan†, Jiawei Liu†, Yuzhu Wang, Hongfei Xu, and Yaozu Liao**

State Key Laboratory of Advanced Fiber Materials, College of Materials Science and Engineering, Donghua University, Shanghai 201620, China.

E-mail: hxu245@dhu.edu.cn (Hongfei Xu), yzliao@dhu.edu.cn (Yaozu Liao)

TABLE OF CONTENTS

1. Supplementary Experimental Section

1.1. Materials

Tris(4-aminophenyl)amine (TPA), Tris(4-aminophenyl)benzene (TPB), 2,4,6-Tris(4-aminophenyl)triazine (TPT), bis(dibenzylideneacetone)palladium ($Pd(dba)_2$), 2-dicyclohexylphosphino-2',4',6'-triisopropylbiphenyl (X-Phos), sodium tert-butoxide (NaOtBu), and 1,3-dibromoazulene were purchased from Shanghai Hao Hong Biological Medicine Technology Co., Ltd. Amino-functionalized carbon nanotubes (CNTs) was purchased from Shenzhen Caron Technology Co., Ltd. Tetrahydrofuran (THF), methanol (MeOH), chloroform ($CHCl_3$), and N,N-dimethylformamide (DMF) were purchased from Shanghai Aladdin Biochemical Technology Co., Ltd. All reagents were used without further purification.

1.2. Preparation of Three CMPs and TPA-CMP@CNT-X

The conjugated microporous polymers (CMPs) were synthesized based on the Buchwald-Hartwig coupling reaction with some changes. TPA (116.1 mg, 0.4 mmol), 1,3-dibromoazulene (171.6 mg, 0.6 mmol), $Pd(dba)_2$ (13.8 mg, 0.024 mmol), X-Phos (17.2 mg, 0.036 mmol), and NaOtBu (173 mg, 1.8 mmol) were added into the Schlenk tube. Anhydrous THF (30 mL) was added into the mixture after vacuum degassing for three times, and then stirred at 65 ℃ for 48 h under a nitrogen atmosphere. The precipitates were purified by filtering and washing with deionized water, MeOH, $CHCl_3$, and DMF. The final products were obtained after vacuum dried at 60 ℃ (TPA-CMP, yield 85%). TPB-CMP (yield 82%) and TPT-CMP (yield 88%) were employed under the same process with corresponding units of TPB (140.5 mg, 0.4 mmol) and TPT (141.8 mg, 0.4 mmol). The TPA-CMP@CNT-X was also prepared under the same process with adding gradient CNT, thereinto, the content of CNT is from 10wt% to 30wt% and 50wt% based on the ratio between CNT and TPA-CMP.

1.3. Materials Characterization

The chemical structures of samples were characterized by Fourier transform infrared (FT-IR, Nicolet IS5, Thermo Fisher), Raman spectra (inVia-Reflex, Renishaw) using an excitation wavelength of 633 nm, and solid-state nuclear magnetic resonance carbon spectrum (^{13}C NMR,

AVANCE 400, Bruker). The crystallinity of all samples was measured by X-ray diffraction (XRD, D8 Advance, Bruker) using Cu Kα radiation (2θ = 5-80°). The *Brunauer-Emmett-Teller* (BET) surface areas with pore size distribution of all samples were tested by nitrogen (N_2) absorption and desorption curve (ASAP 2460, Micromeritics Instrument Corporation) and calculated by the non-local density functional theory (NLDFT). Ultraviolet-Visible Spectroscopy (UV-Vis-DRS) was performed by ultraviolet spectrophotometer (UV-2600i, SHIMADZU). The electron conductivity test was measured by semiconductor tester (2450, Keithley). The morphology of three COFs was obtained by scanning electron microscope (SEM, SU8010, Hitachi) and transmission electron microscope (TEM, Talos F200S, FEI). X-ray photoelectron spectroscopy (XPS, ESCALAB 250Xi, Thermo Fisher) under high vacuum ($1*10^{-9}$ Torr) calibrated to the C1s peak at 284.8 eV and electron paramagnetic resonance (EPR, ELEXSYS, Bruker) were used to evaluate the ion storage mechanism.

1.4. Electrochemical Measurements

The uniform slurry was prepared with 50 wt% active materials (TPA-CMP, TPB-CMP, and TPT-CMP), 40 wt% Ketjen black (KB), and 10 wt% poly(vinylidenefluoride) (PVDF) in n-methylpyrrolidone (NMP), coated on Al foil, dried in a vacuum oven at 60 °C for 8 h, and cut into 12 mm diameter disks for cathode materials with the active material of ~ 0.8 and 1.6 mg cm^{-2}. The CNT electrode was also prepared by mixing 90% CNT and 10 wt% PVDF in NMP, coated on Al foil, dried in a vacuum oven at 60 °C for 8 h, and cut into 12 mm diameter disks for cathode materials with the active material of ~ 1.8 mg cm^{-2}. To ensure the active material consistency, the TPA-CMP@CNT-10, TPA-CMP@CNT-30, and TPA-CMP@CNT-50 electrodes were prepared with ratio of 6:3:1, 7:2:1, and 8:1:1. These electrodes were assembled to CR2032-type coin batteries in an argon-filled glove box (SG1200, Vigor) with Li metal as counter electrode, 1 M $LiPF_6$ in ethylene carbonate (EC): ethyl methyl carbonate (EMC)=3:7 Vol% (80 μL) and polypropylene (PP) as separator for electrochemical performance. The electrochemical performance was evaluated at different current densities from 1.2 to 4.3 V on the NEWARE battery test instrument. The anode was prepared by mixing with 80 wt% graphite, 10 wt% KB, and 10 wt% PVDF in NMP, coated on Cu foil, dried in a vacuum oven at 60 °C

for 8 h, and cut into 12 mm diameter disks for anode materials with the active material of ~ 1.7 mg cm^{-2}. The full-batteries were assembled with TPA-CMP@CNT-50 as cathode (~ 1.6 mg cm^{-2}) and graphite as anode (~ 1.7 mg cm^{-2}). The electrochemical performance was evaluated at different current densities from 1.2 to 4.3 V. The cyclic voltammetry (CV) and electrochemical impedance spectroscopy (EIS) was measured on electrochemical workstation (Interface 1000E, Gamry). The galvanostatic intermittent titration technique (GITT) was detected on NEWARE battery test instrument after 10 cycles at 0.1 A g^{-1} for 10 min and relaxed for 20 min. The Distribution of Relaxation Times (DRT) analysis is conducted using the DRT Tools which are developed by Ciucci. Group (GitHubciuccislab/DRT tools: An intuitive MATLAB GUI to compute the DRT).[1]

1.5. Computational Details

All the molecular simulations were performed using the Gaussian 16 software package[2]. The geometry optimizations and frequency calculations were carried out with the B3LYP hybrid functional[3] and 6-311G(d,p) basis set[4] with Grimme-D3 dispersion corrections[5]. The Solvation Model Based on Density (SMD) of EC/EMC (3:7, v/v) was applied in the calculation. The single point energies were computed at the B3LYP hybrid functional and def2-TZVP basis set[6]. Based on the above data, the binding energy was calculated from the following equation:

$$\triangle E = E_{*ions} - E_{*} - E_{ions}$$

Where *ions present the pristine model of COF binds Li^{+} or PF_6^{-} groups. The HOMO, LUMO, and electrostatic potential analysis were processed using Multiwfn 3.8[7] and visualized by the VMD 1.9.3 package[8].

2. Supplementary Equations

Capacity Contribution Distribution

The capacity contribution could often be classified as two types (pseudo-capacitance and diffusion capacitance), which obey the relationship between the peak current (i) and scan rate (v) is fitted by equation S1:[9]

$$logi = blogv + loga \quad \text{S1}$$

in which a and b are defined as constants. The capacity contribution type can be reflected by the value of b. If the value of b is closed to 0.5, the capacity storage behaviors is mainly based on the diffusion capacitance. If the value of b is closed to 1, the majority of capacity storage is based on the pseudo-capacitance.

Furthermore, the capacity contribution distribution was also calculated by equation S2:[9]

$$i = k_1 v + k_2 v^{1/2} \quad \text{S2}$$

where k_1 and k_2 are constants, and $k_1 v$ and $k_2 v^{1/2}$ represents the contribution of pseudo-capacitance and diffusion capacitance, respectively.

Electronic Conductivities (σ_e)

The σ_e of all samples were measured based on the I-V curves and calculated by the following equation S3:[10]

$$\sigma_e = \frac{L}{R \times A} \quad \text{S3}$$

where L, R, and A are the disc thickness of the COF powder, the slop of I-V curves, and the disc area of the COF powder, respectively.

Ions Diffusion Coefficient (D_{ions})

The D_{ions} were measured by the galvanostatic intermittent titration technique (GITT) on Neware instrument at 0.1 A g^{-1} for 10 min and relaxed for 15 min. The D_{ions} was calculated by the following equation S4:[10]

$$D_{ions} = \frac{4}{\pi\tau}\left(\frac{m_B V_M}{M_B A}\right)^2\left(\frac{\Delta E_s}{\Delta E_\tau}\right)^2 \quad \text{S4}$$

where m_B, V_M, and M_B represent the mass, molar volume, and molecular weight of active material, respectively. A is the contacting area between active material and electrolyte.

Activation Energy (E_a) of electrode

The E_a was calculated from the slope of the Arrhenius plot based on charge transfer resistance (τ_4 and τ_5) at different temperatures from 35 to 60 °C in DRT method by using the equation S5:[10]

$$ln(T/R_{ct}) = (lnA - E_a)/RT \quad \text{S5}$$

where A is the pre-exponential factor, R is the gas constant and T (K) is the testing absolute temperature.

3. Supplementary Figures

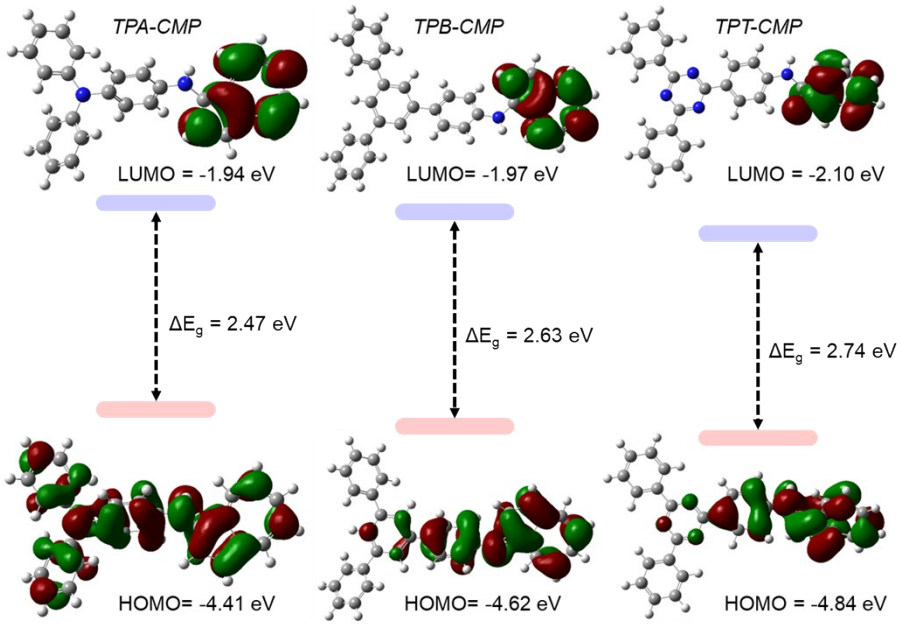

Figure S1. The HOMO-LUMO energy level distribution with energy gap of TPA-CMP, TPB-CMP, and TPT-CMP.

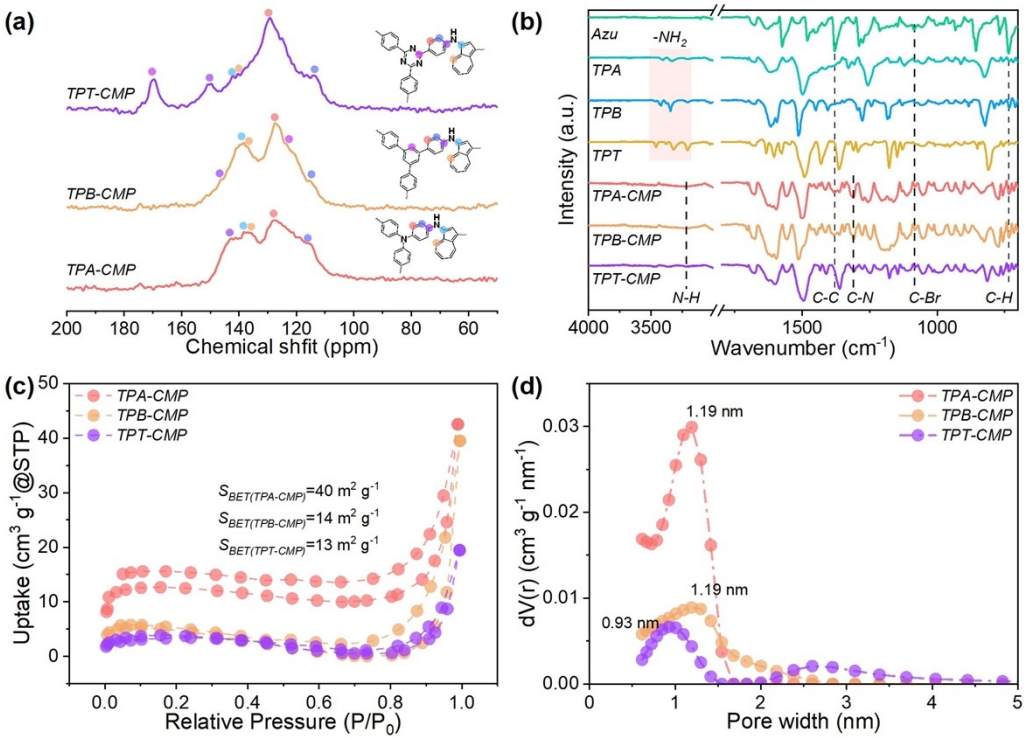

Figure S2. (a) ^{13}C NMR spectra of TPA-CMP, TPB-CMP, and TPT-CMP. (b) FT-IR spectra of TPA-CMP, TPB-CMP, and TPT-CMP with related monomers. (c) N_2 isothermal adsorption/desorption curves with (d) pore size distribution of TPA-CMP, TPB-CMP, and TPT-CMP.

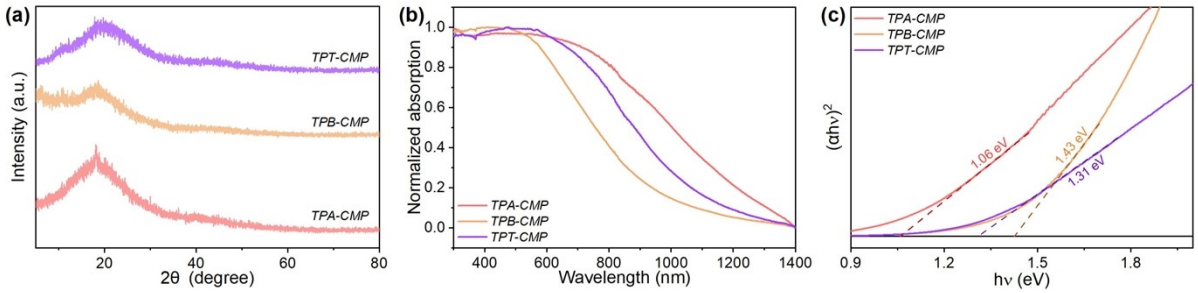

Figure S3. (a) PXRD patterns, (b) UV-Vis diffuse reflectance absorption spectra (DRS), and (c) Tauc plot of TPA-CMP, TPB-CMP, and TPT-CMP.

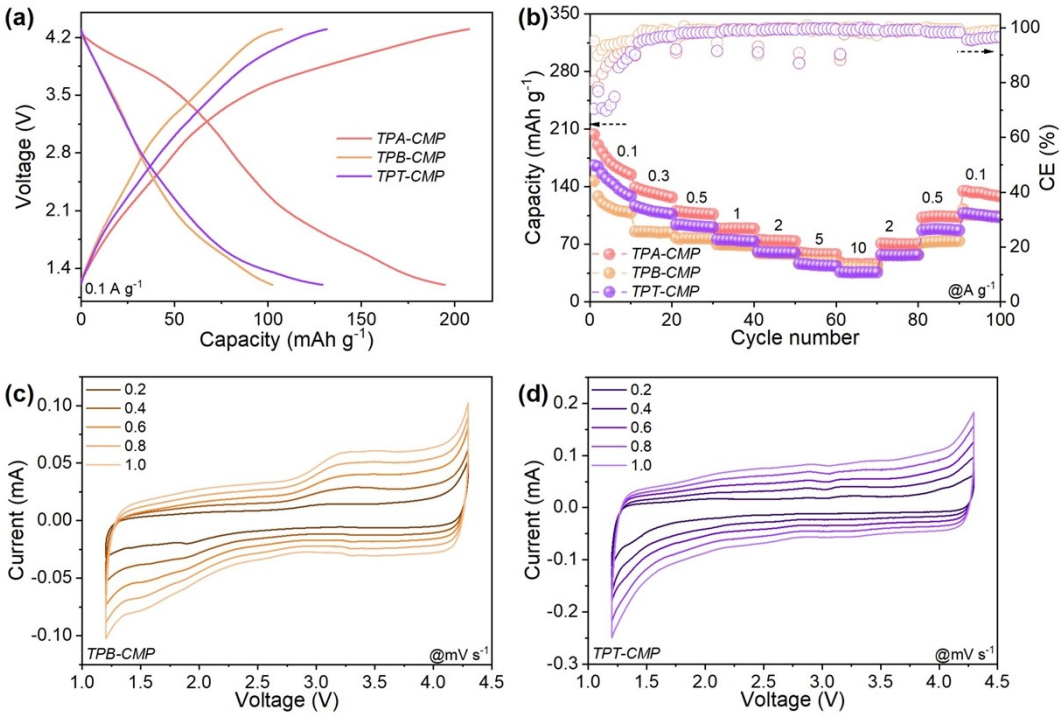

Figure S4. (a) The charge/discharge curves at 0.1 A g^{-1} and (b) rate performance of TPA-CMP, TPB-CMP, and TPT-CMP. The CV curves at different scan rates of (c) TPB-CMP and (d) TPT-CMP.

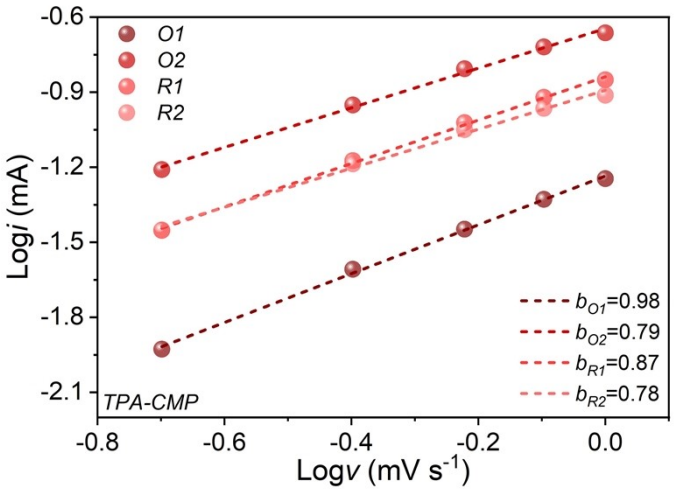

Figure S5. The b values of different redox peaks for TPA-CMP.

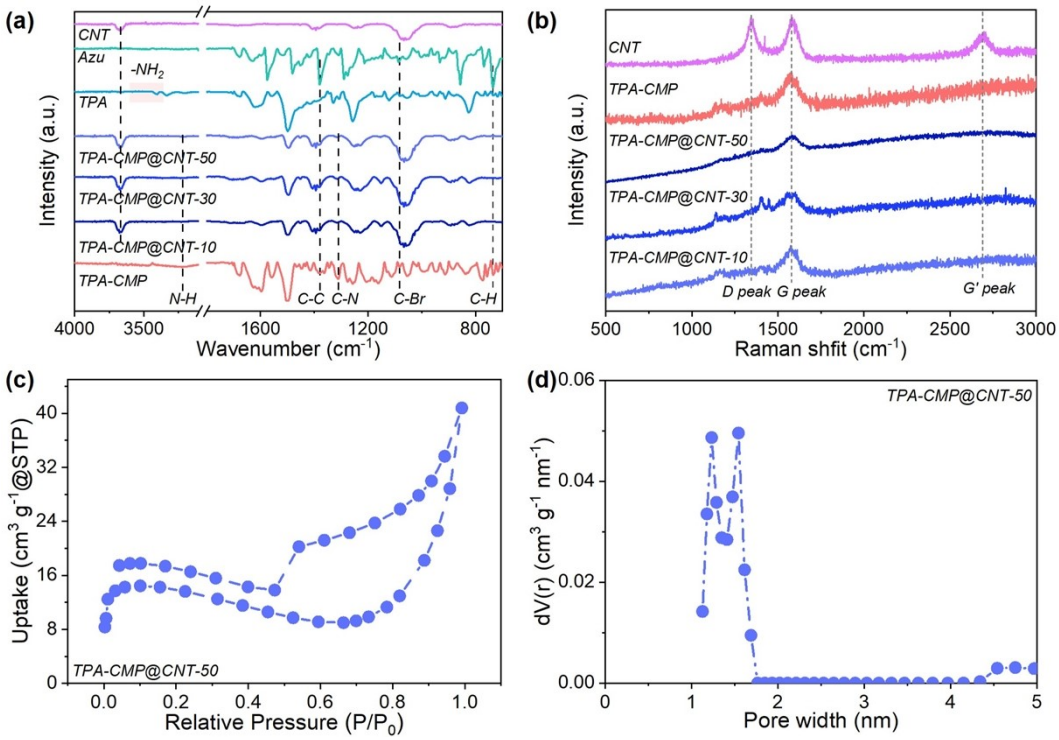

Figure S6. (a) The FT-IR spectra of TPA-CMP and TPA-CMP@CNT-X (X=10, 30, and 50wt%) with related monomers. (b) Raman spectra of CNT, TPA-CMP, and TPA-CMP@CNT-X (X=10, 30, and 50wt%). (c) N_2 isothermal adsorption/desorption curves with (d) pore size distribution of TPA-CMP@CNT-50.

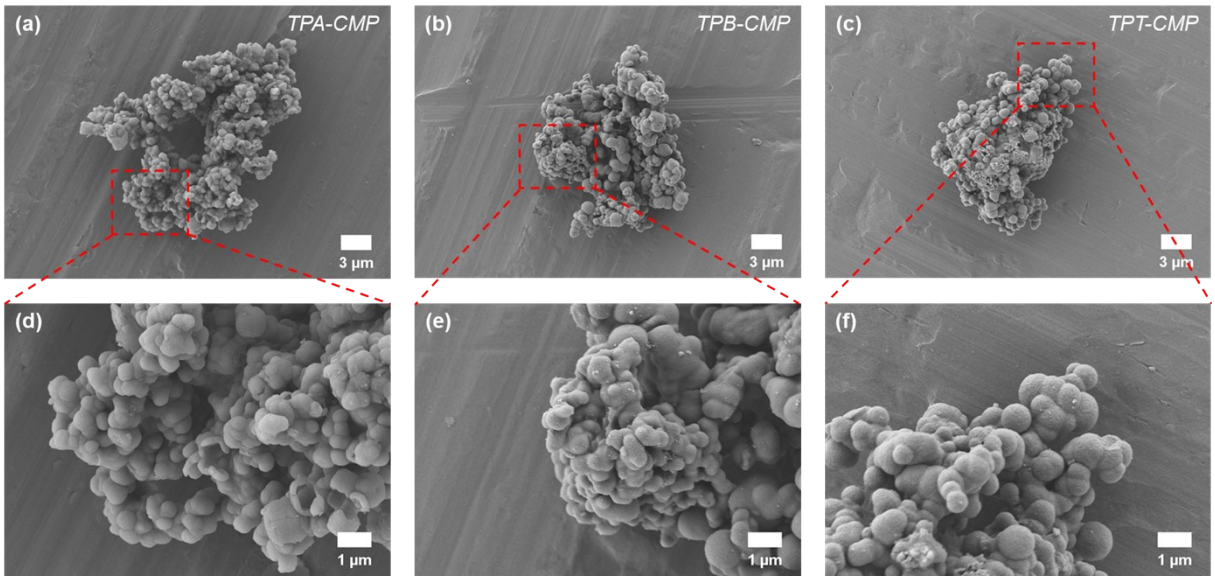

Figure S7. SEM images of (a,d) TPA-CMP, (a,d) TPB-CMP, and (c,f) TPT-CMP.

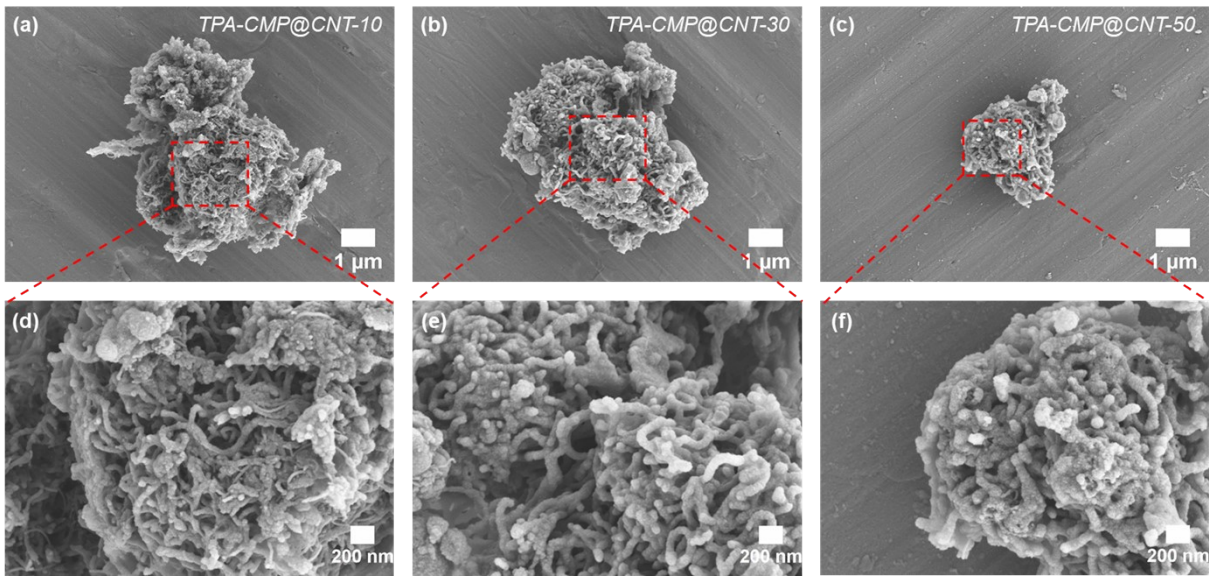

Figure S8. SEM images of (a,d) TPA-CMP@CNT-10, (a,d) TPA-CMP@CNT-30, and (c,f) TPA-CMP@CNT-50.

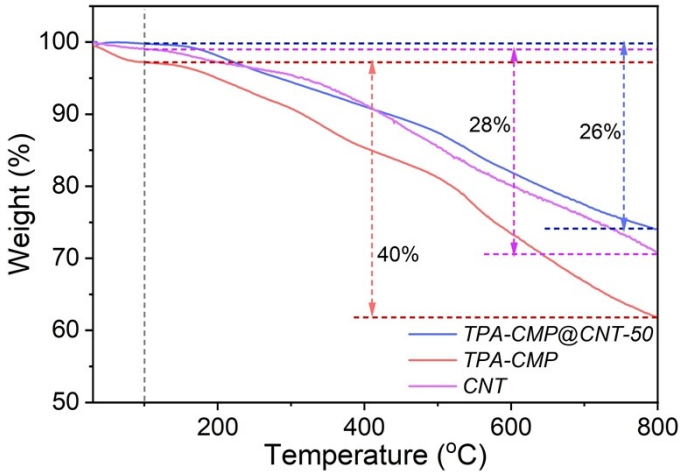

Figure S9. The TGA curves of CNT, TPA-CMP, and TPA-CMP@CNT-50.

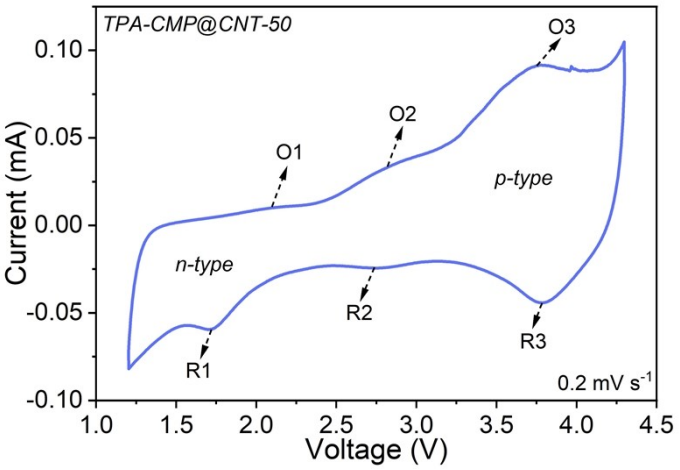

Figure S10. The CV curves of TPA-CMP@CNT-50 at 0.2 mV s^{-1}.

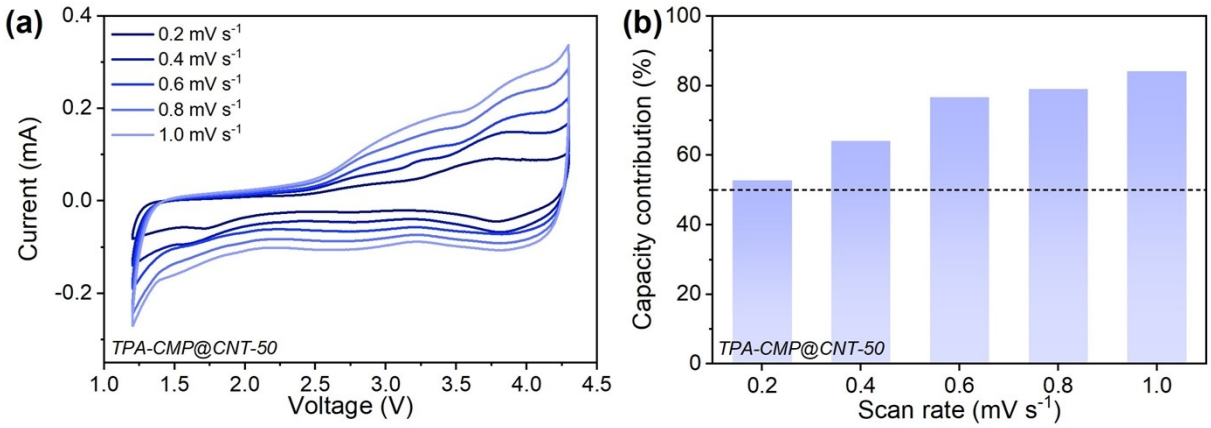

Figure S11. (a) The CV curves and (b) capacitance contribution ratios of TPA-CMP@CNT-50 at different scan rates.

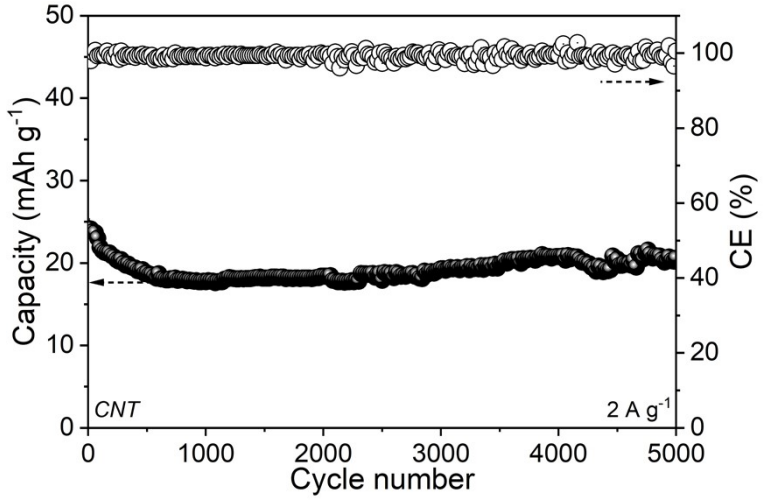

Figure S12. The long-term cycle performance of CNT at 2 A g^{-1}.

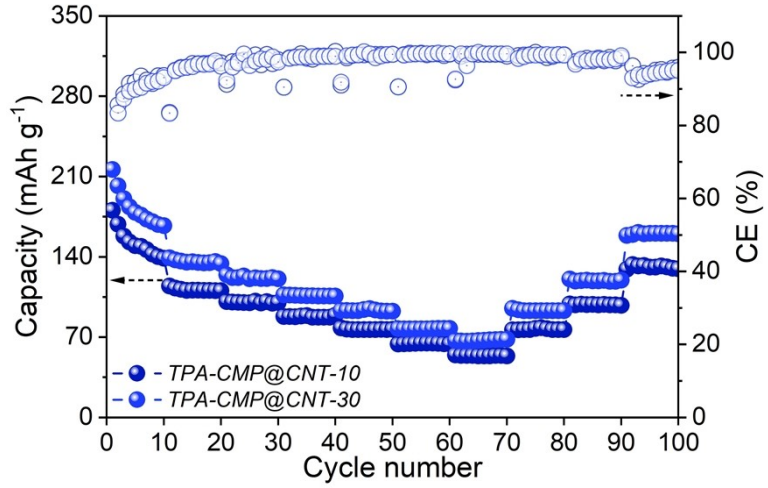

Figure S13. The rate performance of TPA-CMP@CNT-10 and TPA-CMP@CNT-30.

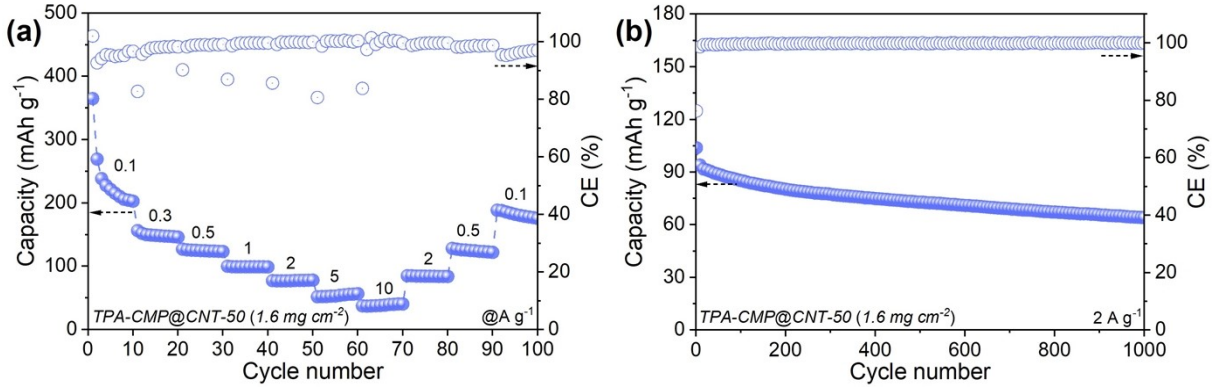

Fig. S14 (a) Rate performance and (b) long-term cycling performance at 2 A g^{-1} of TPA-CMP@CNT-50 with high mass loading of ~ 1.6 mg cm^{-2}.

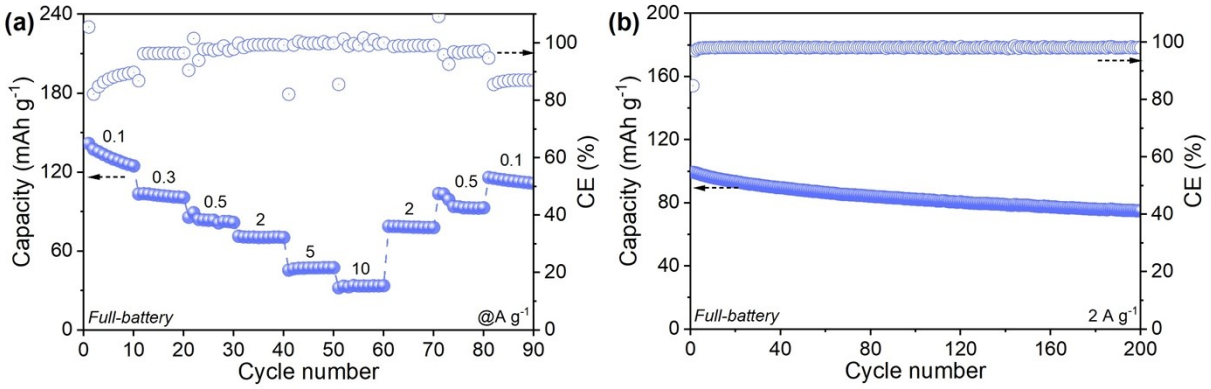

Fig. S15 (a) Rate performance and (b) long-term cycling performance at 2 A g^{-1} of full-battery with TPA-CMP@CNT-50 as cathode and graphite as anode.

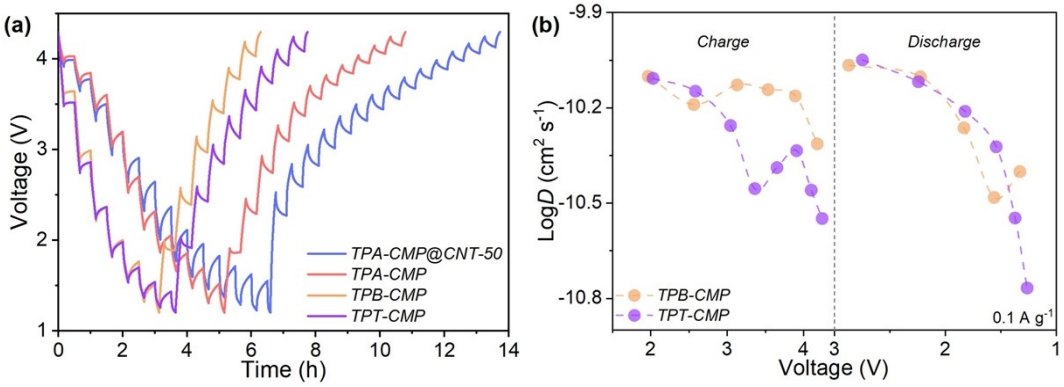

Figure S16. (a) The GITT curves of TPA-CMP, TPB-CMP, TPT-CMP, and TPA-CMP@CNT-50. (b) The ion diffusion coefficients of TPB-CMP and TPT-CMP.

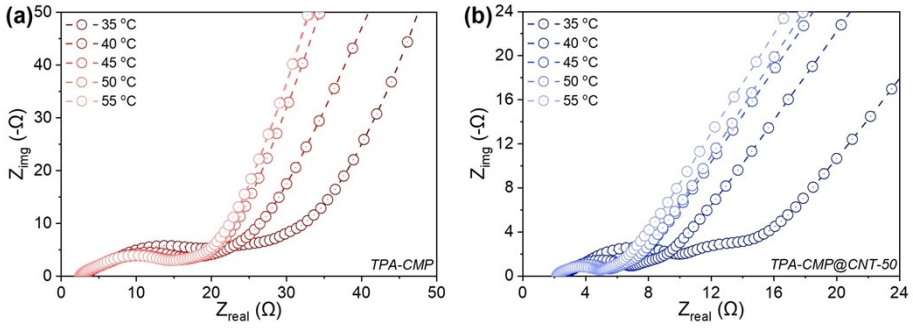

Fig. S17 The Nyquist plots of (a) TPA and (b) TPA-CMP@CNT-50 at various temperatures.

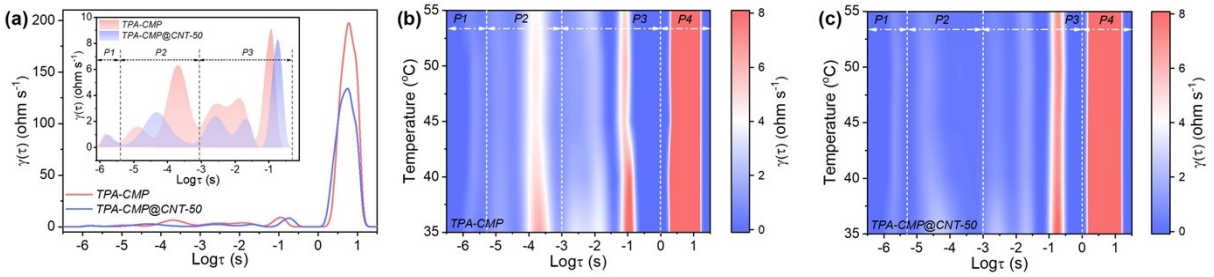

Figure S18. (a) The DRT curves of TPA-CMP and TPA-CMP@CNT-50. The DRT curves of (b) TPA-CMP and (c) TPA-CMP@CNT-50 at different temperatures from 35 to 55 °C. The four regions labelled as P1, P2, P3, and P4 represented the inherent internal resistance, the interfacial resistance, the charge transfer resistance, and the diffusion resistance, respectively.

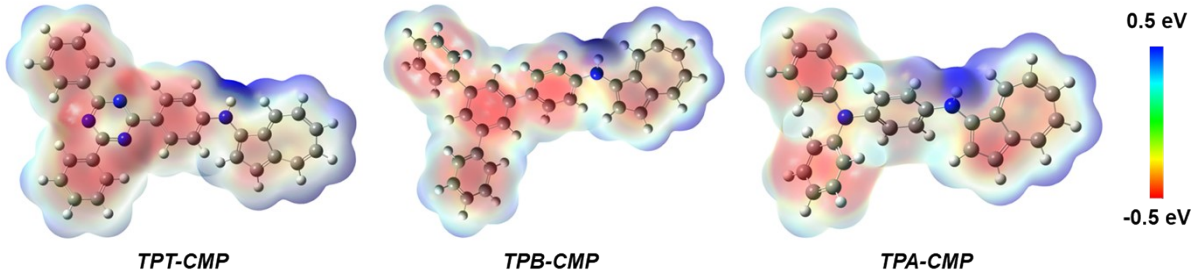

Figure S19. The molecular electrostatic potential surface distribution of TPT-CMP, TPB-CMP, and TPA-CMP.

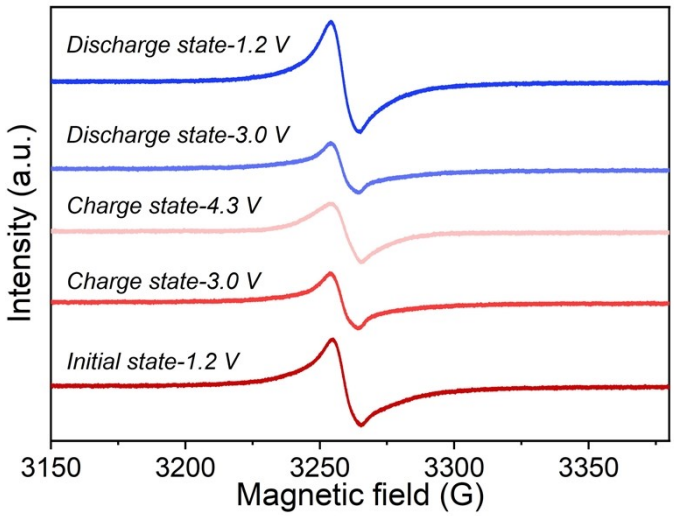

Figure S20. The *ex-situ* electron paramagnetic resonance of TPA-CMP at different voltage state.

4. Supplementary Figures

Table S1. The performance comparison with other recently reported porous polymer cathode materials

Samples	Voltage range	Discharge specific capacity	Capacity retention rate	High-rate capacity	References
TAPP-Pz-COF-40%CNT	1.2-4.4 V	314 mAh g^{-1} (0.2 A g^{-1})	88% (10 A g^{-1}, 10000 cycles)	150 mAh g^{-1} (10 A g^{-1})	*Energy Environ. Sci.* 2024, *17*, 5451
BTT-ICTO@CNT-50	1.0-3.6 V	396 mAh g^{-1} (0.1 A g^{-1})	71% (2 A g^{-1}, 8000 cycles)	227 mAh g^{-1} (20 A g^{-1})	*Angew. Chem. Int. Ed.* 2024, *63*, e202412334
RBT-COF@CNT-50	1.2-4.3 V	302 mAh g^{-1} (0.1 A g^{-1})	80% (2 A g^{-1}, 2000 cycles)	88 mAh g^{-1} (10 A g^{-1})	*Chem. Sci.* 2026, *17*, 5046
HATN-PTO	1.2-3.9 V	330 mAh g^{-1} (0.2 A g^{-1})	49% (5 A g^{-1}, 1000 cycles)	209 mAh g^{-1} (20 A g^{-1})	*Adv. Mater.* 2025, *37*, 2416661
PPCMP	1.2-4.4 V	302 mAh g^{-1} (0.3 A g^{-1})	50% (2 A g^{-1}, 5000 cycles)	109 mAh g^{-1} (5 A g^{-1})	*Chem. Sci.* 2025, *16*, 11311
LPCMP	2.5-4.5 V	147 mAh g^{-1} (0.1 A g^{-1})	96% (0.5 A g^{-1}, 5000 cycles)	83 mAh g^{-1} (20 A g^{-1})	*Adv. Mater.* 2025, *37*, 2410262
PTPAG	1.2-4.2 V	242 mAh g^{-1} (0.1 A g^{-1})	73% (20 A g^{-1}, 10000 cycles)	128 mAh g^{-1} (20 A g^{-1})	*Adv. Energy Mater.* 2026, e06712
TPA-CMP@CNT-50	**1.2-4.3 V**	**242 mAh g^{-1} (0.1 A g^{-1})**	**75% (2 A g^{-1}, 5000 cycles)**	**74 mAh g^{-1} (10 A g^{-1})**	**This work**

Table S2. The related values based on DRT curves of TPA-CMP and TPA-CMP@CNT-50

	TPA-CMP				TPA-CMP@CNT-50			
	P1	**P2**	**P3**	**P4**	**P1**	**P2**	**P3**	**P4**
35 °C	0.4	6.1	8.2	106.1	0.5	2.7	6.1	83.6
40 °C	0.5	5.1	5.7	101.4	0.4	1.5	4.4	80.6
45 °C	0.5	4.6	4.2	99.6	0.4	1.0	4.0	86.2
50 °C	0.5	4.4	4.0	98.9	0.4	1.0	3.9	81.3
55 °C	0.4	4.4	3.9	99.5	0.4	0.8	3.6	85.7

Supplementary References

1 Y. Lu, C.-Z. Zhao, J.-Q. Huang and Q. Zhang, *Joule*, 2022, **6**, 1172-1198.

2 M. J. Frisch, G. W. Trucks, H. B. Schlegel, G. E. Scuseria, M. A. Robb, J. R. Cheeseman, G. Scalmani, V. Barone, G. A. Petersson, H. Nakatsuji, X. Li, M. Caricato, A. V. Marenich, J. Bloino, B. G. Janesko, R. Gomperts, B. Mennucci, H. P. Hratchian, J. V. Ortiz, A. F. Izmaylov, J. L. Sonnenberg, Williams, F. Ding, F. Lipparini, F. Egidi, J. Goings, B. Peng, A. Petrone, T. Henderson, D. Ranasinghe, V. G. Zakrzewski, J. Gao, N. Rega, G. Zheng, W. Liang, M. Hada, M. Ehara, K. Toyota, R. Fukuda, J. Hasegawa, M. Ishida, T. Nakajima, Y. Honda, O. Kitao, H. Nakai, T. Vreven, K. Throssell, J. A. Montgomery Jr., J. E. Peralta, F. Ogliaro, M. J. Bearpark, J. J. Heyd, E. N. Brothers, K. N. Kudin, V. N. Staroverov, T. A. Keith, R. Kobayashi, J. Normand, K. Raghavachari, A. P. Rendell, J. C. Burant, S. S. Iyengar, J. Tomasi, M. Cossi, J. M. Millam, M. Klene, C. Adamo, R. Cammi, J. W. Ochterski, R. L. Martin, K. Morokuma, O. Farkas, J. B. Foresman and D. J. Fox, Gaussian 16, Revision C.01, Gaussian, Inc., Wallingford CT, 2016.

3 A. D. Becke, *J. Chem. Phys.*, 1993, **98**, 5648-5652.

4 W. J. Hehre, R. Ditchfield and J. A. Pople, *J. Chem. Phys.*, 1972, **56**, 2257-2261.

5 C. Bannwarth, S. Ehlert and S. Grimme, *J. Chem. Theory Comput.*, 2019, **15**, 1652-1671.

6 F. Weigend and R. Ahlrichs, *Phys. Chem. Chem. Phys.*, 2005, **7**, 3297-3305.

7 T. Lu and F. Chen, *J. Comput. Chem.*, 2012, **33**, 580-592.

8 W. Humphrey, A. Dalke and K. Schulten, *J. Mol. Graph.*, 1996, **14**, 33-38.

9 J. Duan, K. Wang, L. Teng, H. Liu, L. Xu, Q. Huang, Y. Li, M. Liu, H. Hu, X. Chen, J. Wang, W. Yan, W. Lyu and Y. Liao, *ACS Nano*, 2024, **18**, 29189-29202.

10 J. Duan, L. Teng, H. Liu, X. Zhang, H. Yu, Q. Huang, Y. Li, M. Liu, H. Hu, W. Lyu and Y. Liao, *Angew. Chem. Int. Ed.*, 2025, **64**, e202517853.